Geophysical Research Letters

RESEARCH LETTER
10.1029/2022GL100397

First Simultaneous Lidar Observations of Thermosphere-Ionosphere Sporadic Ni and Na (TISNi and TISNa) Layers (~105–120 km) Over Beijing (40.42°N, 116.02°E)

Fuju Wu[1,2], **Xinzhao Chu**[3], **Lifang Du**[2], **Jing Jiao**[2], **Haoran Zheng**[2], **Yuchang Xun**[2,4], **Wuhu Feng**[5,6], **John M. C. Plane**[5], **and Guotao Yang**[2]

[1]School of Physics, Henan Normal University, Xinxiang, China, [2]State Key Laboratory of Space Weather, National Space Science Center, Chinese Academy of Sciences, Beijing, China, [3]Cooperative Institute of Research in Environmental Sciences & Department of Aerospace Engineering Sciences, University of Colorado Boulder, Boulder, CO, USA, [4]College of Physics and Optoelectronics, Taiyuan University of Technology, Taiyuan, China, [5]School of Chemistry, University of Leeds, Leeds, UK, [6]National Centre for Atmospheric Science (NCAS), University of Leeds, Leeds, UK

Key Points:

- First simultaneous observations of thermosphere-ionosphere sporadic Ni and Na layers (105–120 km) show close correlations and Ni enrichment
- High-density thermosphere-ionosphere sporadic Ni mainly occur in May–June with a maximum of 818 cm^{-3} being 4 times the main Ni peak and correlate well with sporadic E
- Abundance ratios [TISNi]/[TISNa] ~1 and main layer [Ni]/[Na] ~0.1 suggest that direct recombination of Ni^+/Na^+ with electrons produces thermosphere-ionosphere sporadic metal

Supporting Information:

Supporting Information may be found in the online version of this article.

Correspondence to:

X. Chu and G. Yang,
Xinzhao.Chu@Colorado.edu;
gtyang@nssc.ac.cn

Citation:

Wu, F., Chu, X., Du, L., Jiao, J., Zheng, H., Xun, Y., et al. (2022). First simultaneous lidar observations of thermosphere-ionosphere sporadic Ni and Na (TISNi and TISNa) layers (~105–120 km) over Beijing (40.42°N, 116.02°E). *Geophysical Research Letters*, *49*, e2022GL100397. https://doi.org/10.1029/2022GL100397

Received 11 JUL 2022
Accepted 11 AUG 2022

Author Contributions:

Conceptualization: Fuju Wu, Xinzhao Chu
Data curation: Fuju Wu, Lifang Du, Haoran Zheng, Guotao Yang
Formal analysis: Fuju Wu, Xinzhao Chu, Jing Jiao

Abstract

We report the first simultaneous lidar observations of thermosphere-ionosphere sporadic nickel and Na (TISNi and TISNa) layers in altitudes ~105–120 km over Yanqing (40.42°N, 116.02°E), Beijing. From two years of data spanning April 2019 to April 2020 and July 2020 to June 2021, TISNi layers in May and June possess high densities with a maximum of 818 cm^{-3} on 17 May 2021, exceeding the density of main layer peak (~85 km) by ~4 times. They correlate with strong sporadic E layers observed nearby. TISNa layers occur at similar altitudes as TISNi with spatial-temporal correlation coefficients of ~1. The enrichment of Ni in TISNi is evident as the [TISNi]/[TISNa] column abundance ratios are ~1, about 10 times the main layer [Ni]/[Na] ratios. These results are largely explained by neutralization of converged Ni^+ and Na^+ ions via recombination with electrons. Calculations show direct recombination dominating over dissociative recombination above ~105 km.

Plain Language Summary

The metal layers in the Earth's middle and upper atmosphere originate from cosmic dust (i.e., interplanetary dust particles), and they are also called meteoric metal layers. Tons of cosmic dust particles enter the atmosphere each day. Some of these particles heat up during entry to the point where they melt and their metallic constituents begin to vaporize. Na (sodium) is a relatively volatile metal compared to Ni (nickel), so tends to ablate more efficiently. Cosmic dust ablation gives rise to permanent (main) layers of neutral metal atoms which occur globally around 80–100 km in altitude. The Ni layer was observed recently for the first time, and the Ni/Na abundance ratio shown to be ~0.1. In the present study we report the very surprising observations that sporadic layers of these metal atoms, which occur intermittently in the lower thermosphere and ionosphere between 105 and 120 km, have Ni/Na relative abundances which are 10 times larger. We demonstrate that this is likely due to the formation of neutral metals at this height through the process of direct (radiative) recombination of metal ions Ni^+ and Na^+ with electrons. This process is significantly faster for Ni^+ ions.

1. Introduction

The meteoric metal layers in the Earth's upper atmosphere have received growing attention in recent years because of new observational discoveries made by high-sensitivity lidars and other remote sensing instruments (e.g., Chu et al., 2011, 2021; Dawkins et al., 2014; Gao et al., 2015; Langowski et al., 2015, 2017; Raizada et al., 2020), as well as the implementation of metal chemistry, based on laboratory studies of pertinent reactions and meteoric ablation efficiencies, into general circulation models (e.g., Bones et al., 2019, 2020; Chu & Yu, 2017; Daly et al., 2020; Feng et al., 2013; Huba et al., 2019; Plane et al., 2015, 2018). These metal layers are of particular interest for cosmic dust research, and as tracers of atmospheric dynamics, thermal structures, and ion-neutral coupling in the middle/upper atmosphere (e.g., Chu & Yu, 2017; Chu et al., 2011, 2020; Huang et al., 2015; Liu et al., 2016; Plane, 2003, 2012). After nearly a century of ground-based observations of the (permanent) main metal layers (~75–105 km) (e.g., Bernard, 1938; Bowman et al., 1969; Chu & Papen, 2005; Plane, 1991), thermosphere-ionosphere metal (TIMt) layers above the main layers were first discovered in Fe species by lidar

Funding acquisition: Guotao Yang
Investigation: Fuju Wu, Xinzhao Chu, Jing Jiao
Methodology: Fuju Wu, Xinzhao Chu, Jing Jiao, Guotao Yang
Project Administration: Guotao Yang
Resources: Lifang Du, Guotao Yang
Software: Fuju Wu
Supervision: Xinzhao Chu, Guotao Yang
Validation: Xinzhao Chu
Visualization: Fuju Wu
Writing – original draft: Xinzhao Chu
Writing – review & editing: Xinzhao Chu, Yuchang Xun, Wuhu Feng, John M. C. Plane, Guotao Yang

observations in Antarctica (Chu et al., 2011) and then observed globally at all latitudes. By now TIMt layers have been observed by lidars for the metallic species Fe, Na, K, and Ca^+ extending to ∼200 km for neutrals and ∼300 km for Ca^+ (e.g., Chu et al., 2011, 2020, 2021; Friedman et al., 2013; Gao et al., 2015; Jiao et al., 2021; Liu et al., 2016; Lübken et al., 2011; Raizada et al., 2015, 2020; Tsuda et al., 2015; Xun et al., 2019). Most of the neutral TIMt layers exhibit clear signatures of gravity or tidal waves, showing fast downward phase progression (e.g., Chu et al., 2011, 2020, 2021; Gao et al., 2015; Lübken et al., 2011).

At the topside of the main layers and bottomside of the TIMt layers, there exists another interesting phenomenon—the sporadic metal layers between ∼105 and 120 km that are obviously detached from the main layers (like TIMt) but are confined below 125 km with small downward/upward phase speeds. Because they are located in the lower thermosphere and correlate closely with sporadic E layers as shown later, we name these high-altitude sporadic layers the thermosphere-ionosphere sporadic metal (TISMt) layers, to distinguish them from other metal layers. TISMt layers have been observed in Na, Fe, K, and Ca (e.g., Chu et al., 2011; S. C. Collins et al., 1996; Gardner et al., 2001; Gerding et al., 2001; Gong et al., 2003; Höffner & Friedman, 2005; Ma & Yi, 2010; Raizada et al., 2004). These TISMt layers usually have a full-width-at-half-maximum of 5–10 km in altitude, and their peak densities can sometimes be very high, comparable to or exceeding the main-layer peak densities (e.g., Dou et al., 2013; Gardner et al., 2001; Wang et al., 2012; Xue et al., 2013; Yuan et al., 2014).

Lidar observations of neutral nickel (Ni) atoms were made only recently, and are technically challenging. The first two studies of the main Ni layers were made by R. L. Collins et al. (2015) for two nights in Alaska and by Gerding et al. (2019) for six nights in Germany. Large discrepancies were found in peak density (1.6×10^4 vs. $\sim 3 \times 10^2$ cm^{-3}) and column abundance ($\sim 2.7 \times 10^{10}$ vs. $\sim 4 \times 10^8$ cm^{-2}) between them. We then made extensive, year-round lidar observations of the main Ni and Na layers at Yanqing near Beijing (25 nights in Wu et al. (2021) and 126 nights in Jiao et al. (2022)). The main Ni layers at Yanqing have peak density of ∼100–460 cm^{-3}, peak altitude between 80 and 88 km, and column abundance of $(1.52–6.0) \times 10^8$ cm^{-2} (Wu et al., 2021), in good agreement with Gerding et al. (2019). Figure 3 of R. L. Collins et al. (2015) showed one TISNi at ∼110 km on 27–28 November 2012 with its peak density nearly 30% of the main Ni layer peak, but no analysis was done on it. Our observations at Yanqing have revealed many TISNi layers that possess peak densities several times higher than that of the main Ni layers. This paper describes the first simultaneous lidar observations of TISNi and TISNa along with concurrent measurements of sporadic E and the main Ni and Na layers, providing good evidence of plasma-neutral coupling involved in producing the TISMt layers.

2. Concurrent Observations of TISNi and TISNa Layers at Yanqing

A dual-wavelength, broadband resonance-fluorescence lidar, which is part of the Chinese Meridian Project, was used to probe the Ni and Na layers simultaneously at Yanqing (40.42°N, 116.02°E). This lidar consists of two pulsed dye lasers that were pumped by one Nd:YAG laser. One of the dye lasers was frequency doubled to 341.5744 nm (in vacuum) while another one was tuned to 589.1583 nm to excite resonance fluorescence from the Ni($^3D_3 \leftrightarrow {}^3F_4$) and Na D_2 transitions, respectively. Details can be found in Jiao et al. (2015, 2022) and Wu et al. (2021). The raw data were taken at time and vertical resolutions of 33 s and 96 m. The Ni and Na densities were then retrieved with integrated resolutions of 30 min and 960 m, but with an over-sampling step size of 15 min.

2.1. High-Density TISNi and TISNa Layers

Illustrated in Figures 1a and 1b are two examples of strong TISNi layers observed in the ∼105–120 km region on 17 May and 18 June 2021. Both TISNi layers appear to be clearly detached from the main Ni layers between 80 and 95 km. The maximum peak density of the TISNi on 17 May 2021 was ∼818 cm^{-3} at 14.5 UT and ∼106 km (Figure 1e), which is the highest Ni density detected for all altitudes of 80–120 km at Beijing and over 4 times of the peak density (∼200 cm^{-3}) of the main Ni layer during the same night. This strong TISNi layer spanning from ∼103 to 116 km remained at approximately the same altitudes throughout the ∼5-hr observations, with nearly zero phase speed. In contrast, the TISNi on 18 June 2021 exhibited a slow downward phase progression of ∼0.7 m/s. Its maximum peak density was ∼220 cm^{-3} at 13.75 UT and ∼112 km (Figure 1f), lower than Figure 1a but still 1.9 times of the main-layer peak density in Figure 1b. After 15.5 UT, the TISNi and main Ni layers have comparable peak densities.

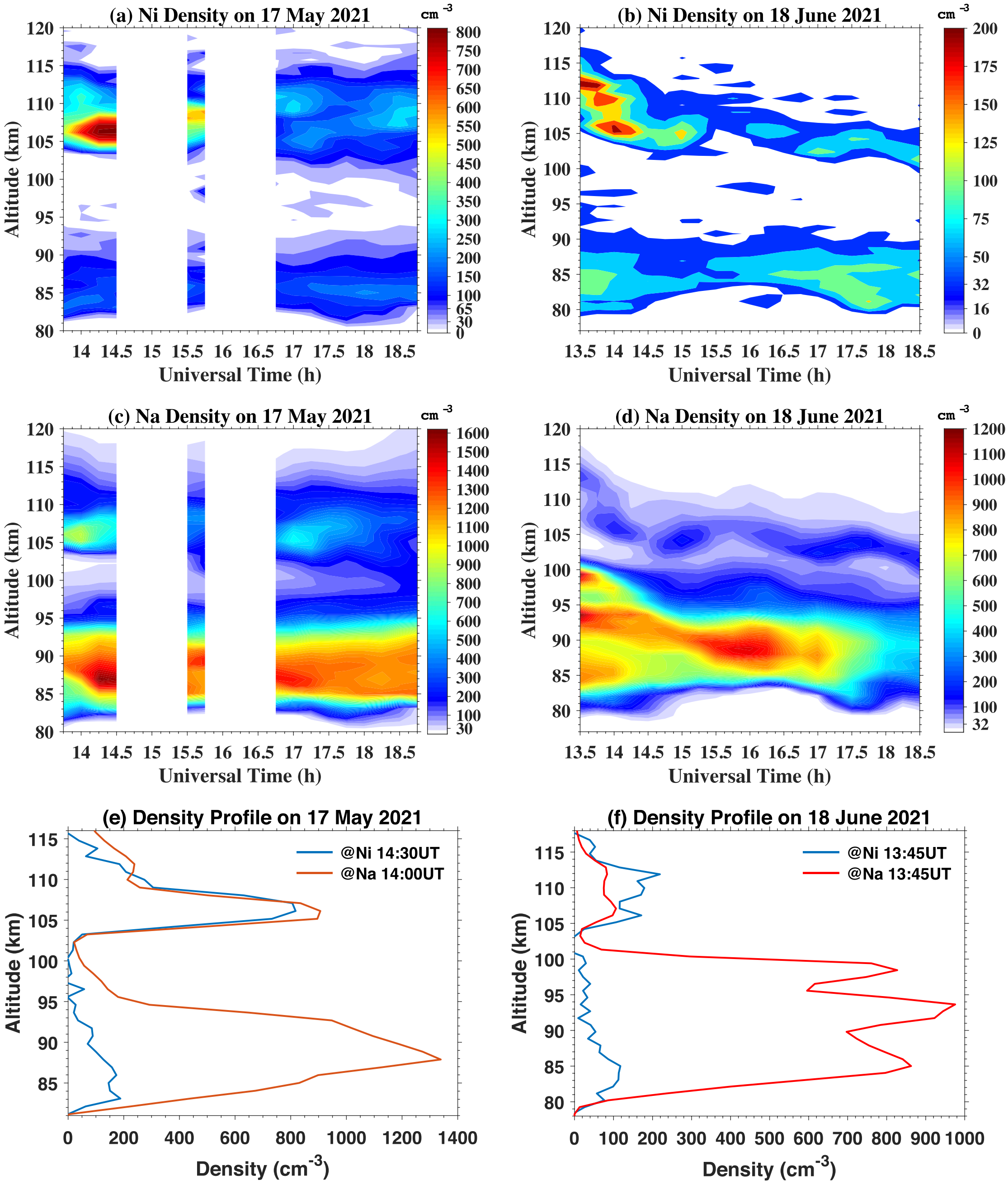
(a) Ni Density on 17 May 2021

(b) Ni Density on 18 June 2021

(c) Na Density on 17 May 2021

(d) Na Density on 18 June 2021

(e) Density Profile on 17 May 2021

(f) Density Profile on 18 June 2021

Figure 1. (a, b) Ni and (c, d) Na number densities from 80 to 120 km on the nights of 17 May 2021 and 18 June 2021, (e, f) vertical profiles of Ni and Na densities.

The corresponding Na measurements are illustrated in Figures 1c and 1d, and two vertical profiles of Na densities are compared to the Ni profiles in Figures 1e and 1f. The TISNa features are strikingly similar to the TISNi layers on both nights, for example, nearly zero phase speed on 17 May 2021 and a slow downward phase progression at ~0.7 m/s with nearly identical layer structures to the TISNi on 18 June 2021. The maximum TISNa density (~900 cm^{-3}) also occurred on 17 May 2021 around 106 km, although slightly earlier (at ~14 UT) than the maximum TISNi occurrence. This maximum TISNa density was ~67% of the peak density of the main Na layers, similar to the findings by Wang et al. (2012) that a strong TISNa layer on 22 May 2010 occupied ~64% of the main-layer peak density at Yanqing.

Such TISMt layers possessing high densities appear frequently, for example, besides the event on 17 May 2021, the TISNi on 26 May 2021 showed nearly 700 cm^{-3} peak density, about 6.4 times higher than that of the main Ni

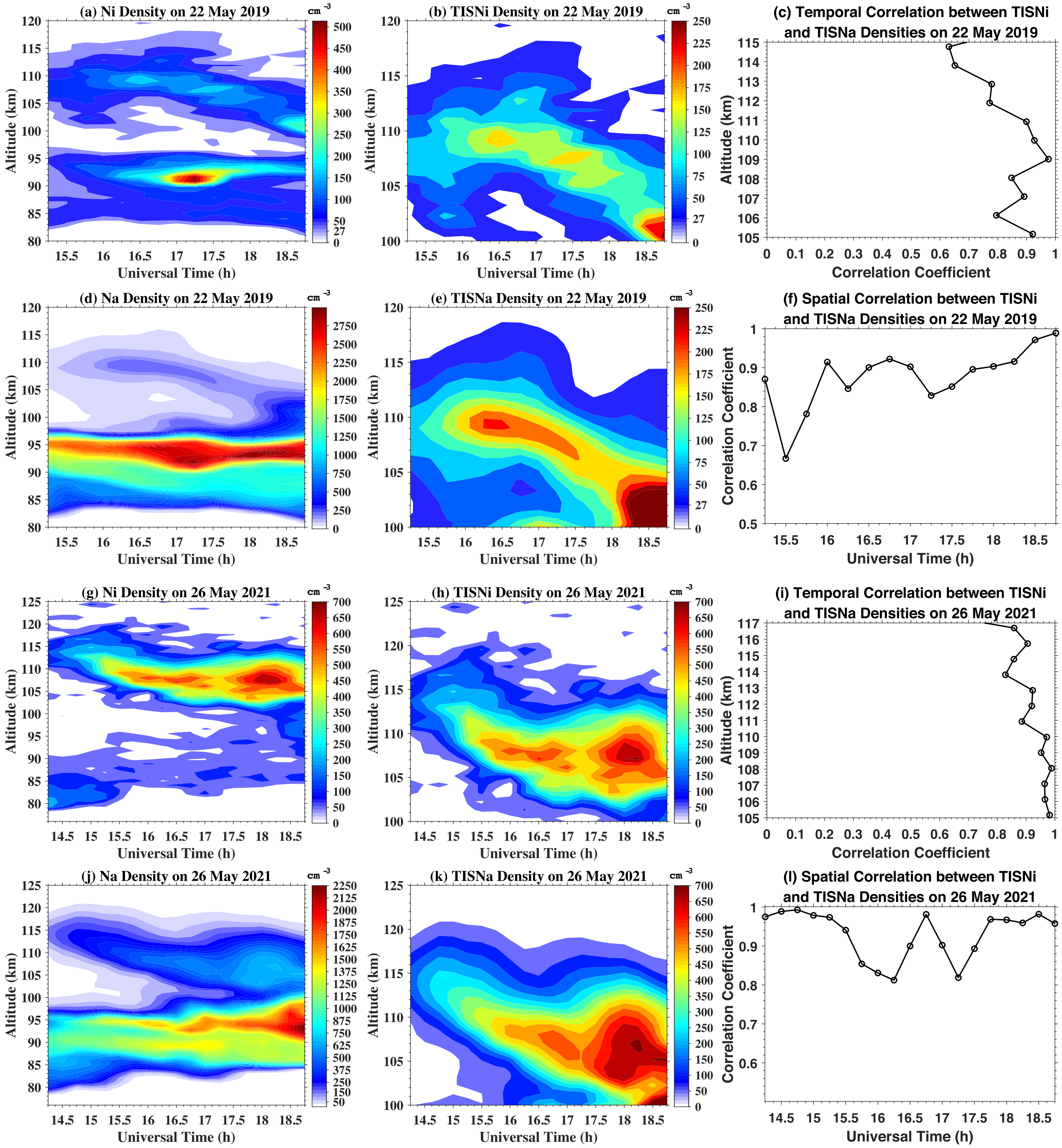

Figure 2. Lidar observations of (left) Ni and Na densities from 80 to 125 km, (middle) thermosphere-ionosphere sporadic Ni and Na (TISNi and TISNa), and (right) the temporal-spatial correlations of TISNi with TISNa variations on 22 May 2019 and 26 May 2021.

layer (see Figure 2). Among the 19 TISNi events identified so far, 8 TISNi layers have their peak densities exceeding the corresponding main Ni layers. The thermosphere-ionosphere sporadic Fe (TISFe) layers observed on 21 June and 21 December 1999 at the North and South Poles, respectively, had peak densities of 2.3×10^5 cm^{-3} and 6,000 cm^{-3} while the peak densities of the main Fe layers were only 1,500–3,000 cm^{-3} (see Figure 1 in Gardner et al., 2001). The current and previous lidar observations demonstrate that both TISNi and TISFe layers can have their peak densities many times higher than those of the corresponding main layers. In contrast, the TISNa peak densities are usually smaller than those of the main Na layers.

2.2. Comparisons of TISNi With TISNa Layers in May and June

A total of 19 TISNi events were identified out of 208 lidar observational nights spanning from April 2019 to April 2020 and from July 2020 to June 2021. All 19 TISNi layers occurred in May–September. Among them, TISNi with high peak densities mainly occurred in May and June, and TISNi appeared on every observational night from 5 May to 8 June. It is necessary to consider the detection threshold for Ni observations because the Ni return signals are 2–3 orders of magnitude smaller than those of Na. The detection threshold can be estimated as 1.5 times of the standard deviation of the background noise from 130 to 160 km, following the method in Gao et al. (2015). With a receiver telescope of ∼1.2 m in diameter and the 341-nm laser power of ∼0.5 W (Wu et al., 2021), the lidar detection thresholds for Ni ranged from ∼10 to ∼215 cm^{-3}, much higher than those for Na (∼0.1–0.75 cm^{-3}). From October through April (∼75% of the total observation time), many nights of observations had high detection thresholds (>35 cm^{-3}) and some nights even reached over 100 or 200 cm^{-3} (likely due to the worsened air quality in winter that attenuates the ultraviolet lidar signals), which were comparable to or even exceed the main Ni layer densities. Therefore, a reasonable conclusion is that TISNi with densities above detection thresholds did not occur outside the period of May through September. However, we cannot rule out the possibility that weak TISNi may occur from October through April.

The 14 TISNi events observed in May and June correlate closely with TISNa. Two examples to demonstrate this are shown in Figure 2. Shown in the left column of Figure 2 are the Ni and Na density contours in the full altitude range of 80–120 km, while the middle column shows only TISNi and TISNa from 100 to 120 km on 22 May 2019 and 26 May 2021. The TISNi and TISNa are strikingly similar in layer peak altitude (ranging from ∼105 to 112 km with a mean at ∼108 km), height distribution, and time evolution of the densities. To quantify the correlation between TISNi and TISNa, we compute the temporal-spatial correlation coefficients between TISNi and TISNa, which are defined as the ratios of the covariance between two density perturbations (calculated by subtracting the nightly mean density) to the product of standard deviations of these two density perturbations (see Equation 3 in Huang et al., 2013). As shown in the right column of Figure 2, both cases exhibit high correlation coefficients close to 1 over the observational time and through the altitude range of 105–120 km, demonstrating the strong correlation between TISNi and TISNa.

Figure 3 displays the peak density ratios and column abundance ratios of TISNi to TISNa in the left and middle columns, while the right column shows the column abundance ratios of the main Ni to Na layers. Despite some variations from night to night, the overall mean [TISNi]/[TISNa] ratios are close to 1, while the main [Ni]/[Na] ratios are close to 0.1. TISNi and TISNa have similar column abundance in 105–120 km, ranging from $\sim 5 \times 10^7$ to $\sim 5 \times 10^8$ cm^{-2} (see Tables S1 and S2 in Supporting Information S1). The mean column abundance of the main Ni and Na layers in May–June is respectively $\sim 2.6 \times 10^8$ and $\sim 3.9 \times 10^9$ cm^{-2} (Jiao et al., 2022). Therefore, the [TISNi]/[TISNa] ratios are ∼10 times of the main layer [Ni]/[Na] ratios.

3. Discussion

The main Ni and Na layers peak around 85 and 92 km, respectively, and main [Ni]/[Na] ratios are ∼0.1, consistent with the results of Jiao et al. (2022). The probable explanations include the more efficient ablation of Na from cosmic dust than Ni, the more rapid neutralization of Na^+ than Ni^+ between 90 and 100 km, and the significant differences in the neutral chemistries of these two metals below 90 km (Jiao et al., 2022). In contrast, the TISNi and TISNa layers have strikingly similar morphologies with temporal-spatial correlations of nearly 1 and [TISNi]/[TISNa] ratios close to 1. These results suggest that the TISNi and TISNa layers share similar formation mechanisms, which are quite different than the main layer formation.

The main Ni and Na layers are formed mainly by release of these metal atoms from the ablation of cosmic dust, with their layer shapes controlled by neutral chemistry on the layer undersides and ion-molecule chemistry on their topsides (Daly et al., 2020; Plane et al., 2015). The metallic ions (Mt^+) are produced during meteoric ablation by collisional ionization, by charge transfer with ambient NO^+ and O_2^+ ions, and (to a lesser extent) by photoionization. We hypothesize that TISMt layers are most likely produced by the neutralization of converged Mt^+ ion layers, due to the high concentration of accompanying electrons, mainly via direct (radiative) recombination ($Mt^+ + e^- \rightarrow Mt$) (Chu & Yu, 2017). This hypothesis is further supported by the observational findings of good correlations between high-altitude sporadic Na layers and sporadic E layers (e.g., Dou et al., 2013; Xue et al., 2013; Yuan et al., 2014). Sporadic E layers mainly consist of metallic ions (e.g., Kopp, 1997; Roddy

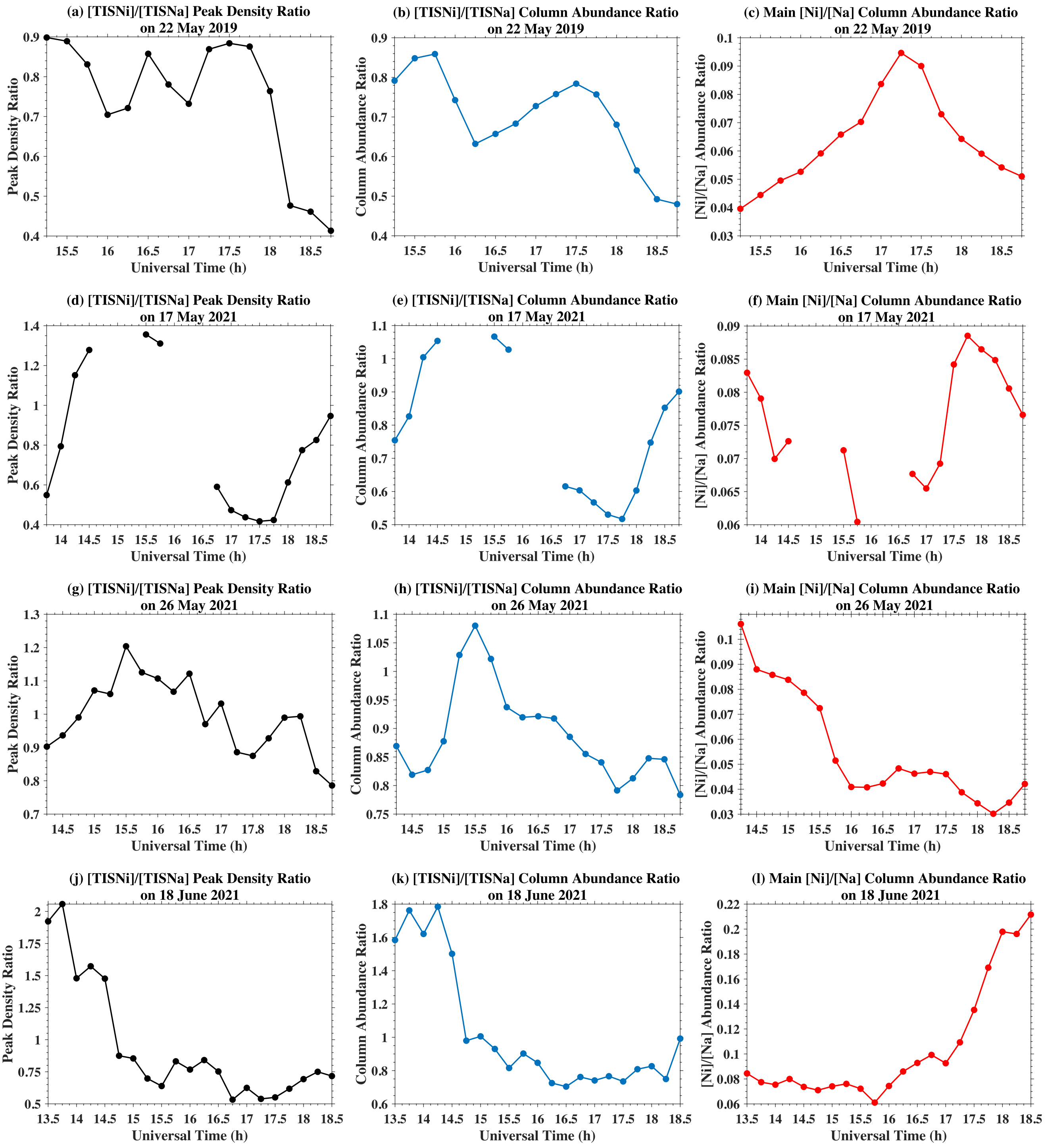

Figure 3. (left) [TISNi]/[TISNa] peak density ratios, (middle) [TISNi]/[TISNa] column abundance ratios, and (right) [Ni]/[Na] column abundance ratios of the main layers on four observational nights.

et al., 2004) that have converged into concentrated layers and have much longer lifetimes than the molecular ions NO^+ and O_2^+ which undergo rapid dissociative electron recombination (e.g., Chu & Yu, 2017; Plane, 2003).

We test this hypothesis by examining concurrent observations of sporadic E layers that were made with an ionosonde at Shisanling (40.3°N, 116.2°E), 28 km away from Yanqing. Strong sporadic E layers with critical frequencies f_oEs greater than 5 MHz were observed simultaneously with all the TISMt events shown in Figures 1 and 2 (see Figure S1 in Supporting Information S1), and several cases have critical frequencies even greater than 10 MHz, reaching ~13 MHz two hours before the strong TISMt events on 17 May 2021 and 18 June 2021 (Figure 1). The corresponding electron concentrations, calculated from the relation $[e^-] \approx 1.24 \times 10^4 \times (f_o\text{Es})^2$ (c m^{-3}), are 3.1×10^5 and 1.24×10^6 cm^{-3} for 5 and 10 MHz, respectively. Rocket-borne measurements have shown that the dominant metal ions in sporadic E layers are Fe^+ while the relative concentrations of Mg^+, Na^+, and Ni^+ are 0.61, 7.41×10^{-2}, and 3.44×10^{-2}, respectively, when normalized to Fe^+ (Kopp, 1997). Assuming that these relative concentrations are reasonably constant in different sporadic E layers and taking into account of all the metal ions listed in Table 2 of Kopp (1997) but neglecting NO^+ and $O_2{}^+$, then the Ni^+ and Na^+ densities relative to the total electron density in a sporadic E layer would be $3.44 \times 10^{-2}/1.77 = 1.94 \times 10^{-2}$ and $7.41 \times 10^{-2}/1.77 = 4.18 \times 10^{-2}$, respectively. The corresponding Ni^+ and Na^+ ion densities would be 6×10^3 and 1.3×10^4 cm^{-3} for a 5-MHz f_oEs and 2.4×10^4 and 5.2×10^4 cm^{-3} for a 10-MHz f_oEs, respectively. Therefore, the Na^+ concentration is ~2.2 times that of Ni^+ within sporadic E layers (Kopp, 1997).

However, the neutralization rate for $Ni^+ \rightarrow Ni$ is larger than that of $Na^+ \rightarrow Na$, which will likely balance out the concentration difference. There are two neutralization paths: direct (radiative) and dissociative recombination with electrons. We are not aware of published high-level quantum mechanical calculations of the thermal rate coefficient for $Ni^+ + e^- \rightarrow Ni + h\nu$. In our previous study we adopted a rate coefficient of $8 \times 10^{-12}(T/300)^{-0.51}$ cm^3 s^{-1}, taken from the analogous reaction of Fe^+ (Daly et al., 2020). However, quantum calculations are available for radiative recombination of $Ni^{2+} + e^- \rightarrow Ni^+$ (Nahar & Bautista, 2001), $Fe^{2+} + e^- \rightarrow Fe^+$ (Nahar, 1997), and $Fe^+ + e^- \rightarrow Fe + h\nu$ (Nahar et al., 1997). The ratio of the radiative recombination rates of Fe^+ and Fe^{2+} is almost constant over the appropriate temperature range (0.43–0.49 between 250 and 500 K). Fe and Ni are both first row transition metals with similar electron configurations ([Ar]3d^{6}4s^2 and [Ar]3d^{8}4s^2, respectively). We have therefore scaled the rate coefficient for Ni^{2+} by the Fe^+/Fe^{2+}, yielding $1.5 \times 10^{-11}(T/300)^{-0.34}$ cm^3 s^{-1}. This should be compared with $2.9 \times 10^{-12}(T/300)^{-0.74}$ cm^3 s^{-1} for $Na^+ + e^- \rightarrow Na + h\nu$ (Plane et al., 2015). At $T = 300$ K, the Ni^+ rate is ~5.2 times faster, likely compensating the lower Ni^+ concentration and leading to comparable TISNi and TISNa densities.

The paths of dissociative recombination for Na^+ and Ni^+ are quite different. Na^+ ions first recombine with N_2 and CO_2 to form cluster ions, which then undergo dissociative recombination with electrons to produce Na (see Table S3 in Supporting Information S1) (Cox & Plane, 1998; Plane et al., 2015). Ni^+ ions react with O_3 and O_2 to form stable oxide ions, which then undergo dissociative recombination with electrons (see Table S4 in Supporting Information S1). However, these oxide ions also react with O, reducing them back to Ni^+ and this process competes with dissociative recombination, thereby slowing the conversion of Ni^+ to Ni. Thus, the relative electron to O concentrations control the rate of dissociative recombination (Bones et al., 2020; Jiao et al., 2022).

Utilizing the WACCM-Ni modeling results of Daly et al. (2020), and taking the mean densities of neutral species near Beijing in May and June (Figure 4d), we compute the first-order neutralization rates of Ni^+ and Na^+ by direct and dissociative recombination for f_oEs of 5–10 MHz. The results are plotted in Figures 4a and 4b for Ni^+ and Na^+, respectively. The ion-molecular reactions applied to the dissociative recombination of Ni^+ and Na^+ (Daly et al., 2020; Jiao et al., 2017; Plane et al., 2015), and the method for calculating the first-order rates (Plane, 2004; Qiu et al., 2021) are detailed in Supporting Information S1.

Neutralization rates increase with the increasing electron density in Figure 4. Dissociative recombination dominates below 100 km, and direct recombination dominates above 105 km. Figure 4c shows the profiles of the direct recombination rate coefficients in the 105–120 km, for which the temperature profile was taken from the average temperature of the WACCM-Ni model (Daly et al., 2020) in May. At the mean peak altitude (~108 km) of TISNi and TISNa, the reaction rates of Ni^+ are ~5 times the Na^+ rates. Considering $[Na^+]/[Ni^+] \approx 2.2$ (Kopp, 1997), the ratio of Ni to Na production rates ($k[Mt^+][e^-]$) is ~2.3, close to the [TISNi]/[TISNa] ratio. The similar formation mechanisms and production rates of TISNi and TISNa also explain why the spatial-temporal correlation coefficients of TISNi and TISNa are close to 1 (Figure 2).

For the highest TISNi density of 818 cm^{-3} observed around ~106 km at 14:30 UT on 17 May 2021, the mean f_oEs in the two hours before it was 10.25 MHz (see Figure S2 in Supporting Information S1). The corresponding $[e^-]$, $[Ni^+]$, and $[Na^+]$ would have been 1.3×10^6, 2.5×10^4, and 5.4×10^4 cm^{-3}, respectively. At ~106 km, the Ni and Na production rates were then ~0.49 and ~0.23 cm^{-3}s^{-1} by direct recombination, and ~0.13 and ~0.14 cm^{-3}s^{-1} by dissociative recombination, respectively. Given 1–2 hr of production, the Ni densities can reach ~1,700–3,500

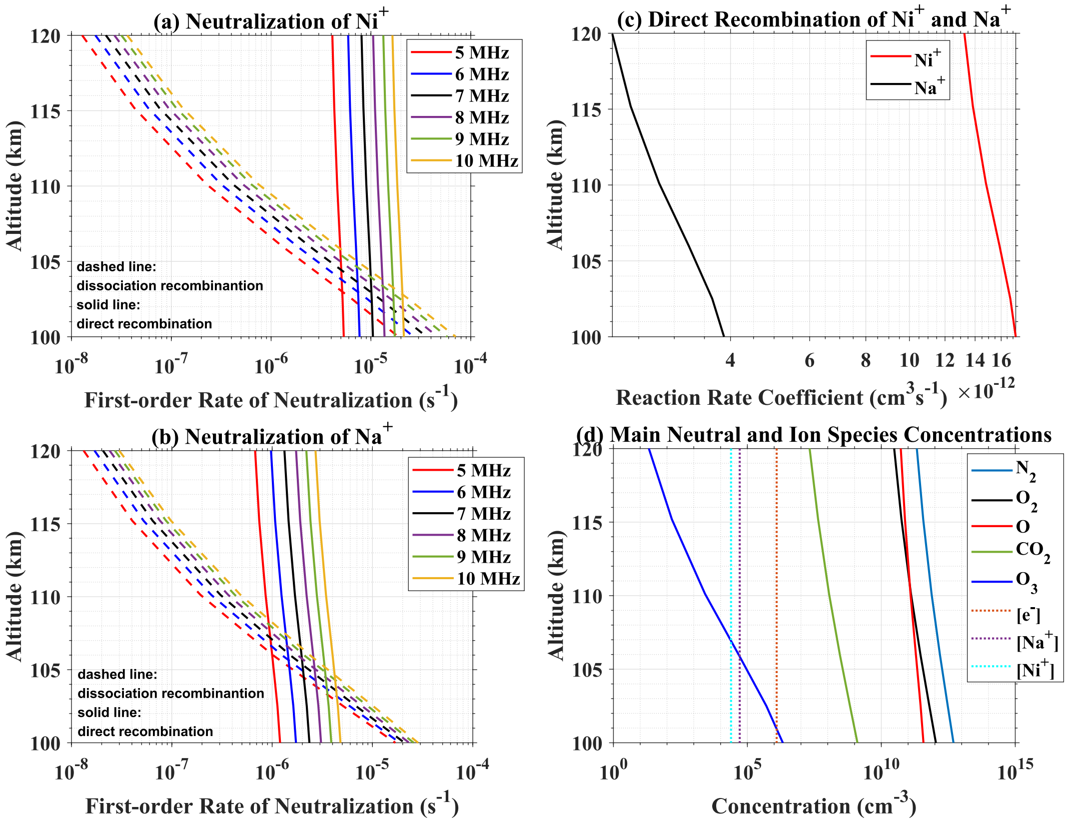

Figure 4. (a, b) The first-order neutralization rates per unit metal ion density for dissociative recombination (dashed lines) and direct recombination (solid lines) of Ni^+ and Na^+ for f_oEs varied from 5 to 10 MHz. (c) The reaction rate coefficients for direct recombination of Ni^+ and Na^+ with electrons. (d) Concentrations of main neutral species and $[e^-]$, $[Ni^+]$, and $[Na^+]$ for $f_o\text{Es} = 10$ MHz used in the calculations.

and ∼450–900 cm^{-3} while the corresponding Na densities are ∼800–1,600 and ∼500–1,000 cm^{-3} for direct and dissociative recombination, respectively. These are comparable to the observed TISNi and TISNa peak densities.

4. Conclusions

In this first report of simultaneous lidar observations of TISNi and TISNa over Yanqing, we have found that these metal layers occur simultaneously in the same altitude range with similar peak densities and temporal-spatial correlation coefficients close to 1. The enrichment of Ni in the TISMt layers is evident as the [TISNi]/[TISNa] column abundance ratios are unity, nearly an order of magnitude higher than the main layer [Ni]/[Na] ratios. High-density TISNi and TISNa layers mainly occur in May and June, and they correspond to strong sporadic E layers with critical frequencies greater than 5 MHz as observed by an ionosonde nearby. Multiple TISNi events have peak densities significantly exceeding (by ∼1.3–6.4 times) that of the main Ni layers, while the TISNa peak densities reach maximum ∼67% of the main Na layers. Back-of-the-envelope calculations provide good evidence that the TISNi and TISNa are formed by the neutralization of converged Ni^+ and Na^+ ions in the sporadic E layers via recombination with electrons, and direct recombination dominates over dissociative recombination above ∼105 km. The lower Ni^+ concentration is compensated by the higher direct-recombination rate coefficient of Ni^+ when compared to Na^+, thus leading to similar Ni and Na production rates. The highest peak density 818 cm^{-3} of TISNi observed on 17 May 2021 is comfortably explained by the strong sporadic E layer with ∼10 MHz f_oEs that occurred 1–2 hr before the lidar observations.

Detailed modeling that includes chemical production and loss reactions, ion and neutral transport, and the meteoric input flux will be necessary to fully understand the observations. While the TISMt and TIMt layers appear to share the same origins (i.e., neutralization of converged Mt^+ ions), it is still puzzling why TISMt layers remain below ~120 km but sometimes possess very high densities while TIMt layers can reach much higher up (~200 km) with large downward phase speeds. Mechanisms of ion transport/convergence should be considered in future modeling. The question of why TISMt layers occur most frequently in May and June with the highest densities, which is likely related to the abnormally high occurrence of sporadic E layers during summer in the Asian sector (e.g., Smith, 1978), deserves future studies. Global observations are necessary to explore these open questions. Such TISMt and TIMt studies call for development of high-sensitivity metal lidars to enable new science endeavors.

Data Availability Statement

Sporadic E data were provided by Beijing National Observatory of Space Environment, IGGCAS through the Geophysics Center, National Earth System Science Data Center (http://wdc.geophys.ac.cn). The data shown in this work, including the sporadic E data shown in Figure S1 in Supporting Information S1, can be downloaded in MatLab data format from Mendeley Data repository (Wu et al., 2022, https://doi.org/10.17632/scnxzsyj92.2).

Acknowledgments
We gratefully acknowledge Xuewu Cheng, Jihong Wang, Faqun Li, and Yong Yang for their contributions to the dual-wavelength lidar development. This work was supported by Youth Innovation Promotion Association of CAS (2019150), NSFC (42004134, 41627804), and Chinese Meridian Project. XC was supported by USA National Science Foundation grants OPP-1246405, OPP-1443726, OPP-2110428, and AGS-1452351. WF and JMCP were supported by UK National Environment Research Council Grant NE/P001815/1.

References

Bernard, R. (1938). Sodium in the high atmosphere. *Nature*, *141*(3574), 788. https://doi.org/10.1038/141788a0

Bones, D. L., Carrillo-Sánchez, J. D., Kulak, A. N., & Plane, J. M. C. (2019). Ablation of Ni from micrometeoroids in the upper atmosphere: Experimental and computer simulations and implications for Fe ablation. *Planetary and Space Science*, *179*, 104725. https://doi.org/10.1016/j.pss.2019.104725

Bones, D. L., Daly, S., Mangan, T. P., & Plane, J. M. C. (2020). A Study of the reactions of Ni^+ and NiO^+ ions relevant to planetary upper atmospheres. *Physical Chemistry Chemical Physics*, *22*(16), 8940–8951. https://doi.org/10.1039/D0CP01124J

Bowman, M. R., Gibson, A. J., & Sandford, M. C. W. (1969). Atmospheric sodium measured by a tuned laser radar. *Nature*, *221*(5179), 456–457. https://doi.org/10.1038/221456a0

Chu, X., Chen, Y., Cullens, C. Y., Yu, Z., Xu, Z., Zhang, S.-R., et al. (2021). Mid-latitude thermosphere-ionosphere Na (TINa) layers observed with high-sensitivity Na Doppler lidar over Boulder (40.13°N, 105.24°W). *Geophysical Research Letters*, *48*(11), e2021GL093729. https://doi.org/10.1029/2021GL093729

Chu, X., Nishimura, Y., Xu, Z., Yu, Z., Plane, J. M. C., Gardner, C. S., & Ogawa, Y. (2020). First simultaneous lidar observations of thermosphere-ionosphere Fe and Na (TIFe and TINa) layers at McMurdo (77.84°S, 166.67°E), Antarctica with concurrent measurements of aurora activity, enhanced ionization layers, and converging electric field. *Geophysical Research Letters*, *47*(20), e2020GL090181. https://doi.org/10.1029/2020GL090181

Chu, X., & Papen, G. C. (2005). Resonance fluorescence lidar for measurements of the middle and upper atmosphere. In T. Fujii & T. Fukuchi (Eds.), *Laser remote sensing* (pp. 179–432). CRC Press, Taylor and Francis.

Chu, X., & Yu, Z. (2017). Formation mechanisms of neutral Fe layers in the thermosphere at Antarctica studied with a thermosphere-ionosphere Fe/Fe^+ (TIFe) model. *Journal of Geophysical Research: Space Physics*, *122*(6), 6812–6848. https://doi.org/10.1002/2016JA023773

Chu, X., Yu, Z., Gardner, C. S., Chen, C., & Fong, W. (2011). Lidar observations of neutral Fe layers and fast gravity waves in the thermosphere (110–155 km) at McMurdo (77.8°S, 166.7°E), Antarctica. *Geophysical Research Letters*, *38*(23), L23807. https://doi.org/10.1029/2011GL050016

Collins, R. L., Li, J., & Martus, C. M. (2015). First lidar observation of the mesospheric nickel layer. *Geophysical Research Letters*, *42*(2), 665–671. https://doi.org/10.1002/2014GL062716

Collins, S. C., Hallinan, T. J., Smith, R. W., & Hernandez, G. (1996). Lidar observations of a large high-altitude sporadic Na during active aurora. *Geophysical Research Letters*, *23*(24), 3655–3658. https://doi.org/10.1029/96GL03337

Cox, R. M., & Plane, J. M. C. (1998). An ion-molecule mechanism for the formation of neutral sporadic Na layers. *Journal of Geophysical Research*, *103*(D6), 6349–6359. https://doi.org/10.1029/97JD03376

Daly, S. M., Feng, W., Mangan, T. P., Gerding, M., & Plane, J. M. C. (2020). The meteoric Ni layer in the upper atmosphere. *Journal of Geophysical Research: Space Physics*, *125*(8), e2020JA028083. https://doi.org/10.1029/2020JA028083

Dawkins, E. C. M., Plane, J. M. C., Chipperfield, M. P., Feng, W., Gumbel, J., Hedin, J., et al. (2014). First global observations of the mesospheric potassium layer. *Geophysical Research Letters*, *41*(15), 5653–5661. https://doi.org/10.1002/2014GL060801

Dou, X. K., Qiu, S. C., Xue, X. H., Chen, T. D., & Ning, B. Q. (2013). Sporadic and thermospheric enhanced sodium layers observed by a lidar chain over China. *Journal of Geophysical Research: Space Physics*, *118*(10), 6627–6643. https://doi.org/10.1002/jgra.50579

Feng, W., Marsh, D. R., Chipperfield, M. P., Janches, D., Höffner, J., Yi, F., & Plane, J. M. C. (2013). A global atmospheric model of meteoric iron. *Journal of Geophysical Research: Atmospheres*, *118*(16), 9456–9474. https://doi.org/10.1002/jgrd.50708

Friedman, J. S., Chu, X., Brum, C. G. M., & Lu, X. (2013). Observation of a thermospheric descending layer of neutral K over Arecibo. *Journal of Atmospheric and Solar-Terrestrial Physics*, *104*, 253–259. https://doi.org/10.1016/j.jastp.2013.03.002

Gao, Q., Chu, X., Xue, X., Dou, X., Chen, T., & Chen, J. (2015). Lidar observations of thermospheric Na layers up to 170 km with a descending tidal phase at Lijiang (26.7°N, 100.0°E), China. *Journal of Geophysical Research: Space Physics*, *120*(10), 9213–9220. https://doi.org/10.1002/2015JA021808

Gardner, C. S., Papen, G. C., Chu, X., & Pan, W. (2001). First lidar observations of middle atmosphere temperatures, Fe densities, and polar mesospheric clouds over the North and South Poles. *Geophysical Research Letters*, *28*(7), 1199–1202. https://doi.org/10.1029/2000GL012622

Gerding, M., Alpers, M., Höffner, J., & von Zahn, U. (2001). Sporadic Ca and Ca^+ layers at mid-latitudes: Simultaneous observations and implications for their formation. *Annales Geophysicae*, *19*(1), 47–58. https://doi.org/10.5194/angeo-19-47-2001

Gerding, M., Daly, S., & Plane, J. M. C. (2019). Lidar soundings of the mesospheric nickel layer using $Ni(^3F)$ and $Ni(^3D)$ transitions. *Geophysical Research Letters*, *46*(1), 408–415. https://doi.org/10.1029/2018GL080701

Gong, S. S., Yang, G. T., Wang, J. H., Cheng, X. W., Li, F. Q., & Wan, W. X. (2003). A double sodium layer event observed over Wuhan, China by lidar. *Geophysical Research Letters*, *30*(5), 1209. https://doi.org/10.1029/2002GL016135

Höffner, J., & Friedman, J. S. (2005). The mesospheric metal layer topside: Examples of simultaneous metal observations. *Journal of Atmospheric and Solar-Terrestrial Physics*, *67*(13), 1226–1237. https://doi.org/10.1016/j.jastp.2005.06.010

Huang, W., Chu, X., Gardner, C. S., Carrillo-Sánchez, J. D., Feng, W., Plane, J. M. C., & Nesvorny, D. (2015). Measurements of the vertical fluxes of atomic Fe and Na at the mesopause: Implications for the velocity of cosmic dust entering the atmosphere. *Geophysical Research Letters*, *42*(1), 169–175. https://doi.org/10.1002/2014GL062390

Huang, W., Chu, X., Gardner, C. S., Wang, Z., Fong, W., Smith, J. A., & Roberts, B. R. (2013). Simultaneous, common-volume lidar observations and theoretical studies of correlations among Fe/Na layers and temperatures in the mesosphere and lower thermosphere at Boulder Table Mountain (40°N, 105°W), Colorado. *Journal of Geophysical Research: Atmospheres*, *118*(15), 8748–8759. https://doi.org/10.1002/jgrd.50670

Huba, J. D., Krall, J., & Drob, D. (2019). Global ionospheric metal ion transport with SAMI3. *Geophysical Research Letters*, *46*(14), 7937–7944. https://doi.org/10.1029/2019GL083583

Jiao, J., Feng, W., Wu, F., Wu, F., Zheng, H., Du, L., et al. (2022). A Comparison of the midlatitude nickel and sodium layers in the mesosphere: Observations and modeling. *Journal of Geophysical Research: Space Physics*, *127*(2), e2021JA030170. https://doi.org/10.1029/2021JA030170

Jiao, J., Jin, H., Yang, G., Yan, C., & Du, L. (2021). *First lidar observations of TICa+ layers in the ionosphere F region up to ~300 km at Beijing (40.42°N, 116.02°E). China*. In *Paper presented at the American Geophysical Union (AGU) fall meeting*.

Jiao, J., Yang, G., Wang, J., Cheng, X., Li, F., Yang, Y., et al. (2015). First report of sporadic K layers and comparison with sporadic Na layers at Beijing, China (40.6°N, 116.2°E). *Journal of Geophysical Research: Atmospheres*, *120*(6), 5214–5225. https://doi.org/10.1002/2014JA020955

Jiao, J., Yang, G., Wang, J., Feng, W., & Plane, J. M. C. (2017). Observations of dramatic enhancements to the mesospheric K layer. *Geophysical Research Letters*, *44*(24), 12536–12542. https://doi.org/10.1002/2017GL075857

Kopp, E. (1997). On the abundance of metal ions in the lower ionosphere. *Journal of Geophysical Research*, *102*(A5), 9667–9674. https://doi.org/10.1029/97JA00384

Langowski, M. P., von Savigny, C., Burrows, J. P., Feng, W., Plane, J. M. C., Marsh, D. R., et al. (2015). Global investigation of the Mg atom and ion layers using SCIAMACHY/Envisat observations between 70 and 150 km altitude and WACCM-Mg model results. *Atmospheric Chemistry and Physics*, *15*(1), 273–295. https://doi.org/10.5194/acp-15-273-2015

Langowski, M. P., von Savigny, C., Burrows, J. P., Fussen, D., Dawkins, E. C. M., Feng, W., et al. (2017). Comparison of global datasets of sodium densities in the mesosphere and lower thermosphere from GOMOS, SCIAMACHY and OSIRIS measurements and WACCM model simulations from 2008 to 2012. *Atmospheric Measurement Techniques*, *10*(8), 2989–3006. https://doi.org/10.5194/amt-10-2989-2017

Liu, A. Z., Guo, Y., Vargas, F., & Swenson, G. R. (2016). First measurement of horizontal wind and temperature in the lower thermosphere (105–140 km) with a Na Lidar at Andes Lidar Observatory. *Geophysical Research Letters*, *43*(6), 2374–2380. https://doi.org/10.1002/2016GL068461

Lübken, F. J., Höffner, J., Viehl, T. P., Kaifler, B., & Morris, R. J. (2011). First measurements of thermal tides in the summer mesopause region at Antarctic latitudes. *Geophysical Research Letters*, *38*(24), L24806. https://doi.org/10.1029/2011GL050045

Ma, Z., & Yi, F. (2010). High-altitude sporadic metal atom layers observed with Na and Fe lidars at 30°N. *Journal of Atmospheric and Solar-Terrestrial Physics*, *72*(5–6), 482–491. https://doi.org/10.1016/j.jastp.2010.01.005

Nahar, S. N. (1997). Electron-ion recombination of Fe II. *Physical Review A*, *55*(3), 1980–1987. https://doi.org/10.1103/PhysRevA.55.1980

Nahar, S. N., & Bautista, M. A. (2001). Electron-ion recombination rate coefficients and photoionization cross sections for astrophysically abundant elements. VI. Ni II. *The Astrophysical Journal Supplement Series*, *137*(1), 201–2017. https://doi.org/10.1086/322540

Nahar, S. N., Bautista, M. A., & Pradhan, A. K. (1997). Electron-ion recombination of neutral iron. *The Astrophysical Journal*, *479*(1), 497–503. https://doi.org/10.1086/303874

Plane, J. M. C. (1991). The chemistry of meteoric metals in the Earth's upper atmosphere. *International Reviews in Physical Chemistry*, *10*(1), 55–106. https://doi.org/10.1080/01442359109353254

Plane, J. M. C. (2003). Atmospheric chemistry of meteoric metals. *Chemical Reviews*, *103*(12), 4963–4984. https://doi.org/10.1021/cr0205309

Plane, J. M. C. (2004). A new time-resolved model of the mesospheric Na layer: Constraints on the meteor input function. *Atmospheric Chemistry and Physics Discussions*, *4*(3), 39–69. https://doi.org/10.5194/acp-4-627-2004

Plane, J. M. C. (2012). Cosmic dust in the Earth's atmosphere. *Chemical Society Reviews*, *41*(19), 6507–6518. https://doi.org/10.1039/c2cs35132c

Plane, J. M. C., Feng, W., & Dawkins, E. C. M. (2015). The mesosphere and metals: Chemistry and changes. *Chemical Reviews*, *115*(10), 4497–4541. https://doi.org/10.1021/cr500501m

Plane, J. M. C., Feng, W., Gómez Martín, J. C., Gerding, M., & Raizada, S. (2018). A new model of meteoric calcium in the mesosphere and lower thermosphere. *Atmospheric Chemistry and Physics*, *18*(20), 14799–14811. https://doi.org/10.5194/acp-18-14799-2018

Qiu, S., Wang, N., Soon, W., Lu, G., Jia, M., Wang, X., et al. (2021). The sporadic sodium layer: A possible tracer for the conjunction between the upper and lower atmospheres. *Atmospheric Chemistry and Physics*, *21*(15), 11927–11940. https://doi.org/10.5194/acp-21-11927-2021

Raizada, S., Brum, C. M., Tepley, C. A., Lautenbach, J., Friedman, J. S., Mathews, J. D., et al. (2015). First simultaneous measurements of Na and K thermospheric layers along with TILs from Arecibo. *Geophysical Research Letters*, *42*(23), 10106–10112. https://doi.org/10.1002/2015GL066714

Raizada, S., Smith, J. A., Lautenbach, J., Aponte, N., Perillat, P., Sulzer, M., & Mathews, J. D. (2020). New lidar observations of Ca^+ in the mesosphere and lower thermosphere over Arecibo. *Geophysical Research Letters*, *47*(5), e2020GL087113. https://doi.org/10.1029/2020GL087113

Raizada, S., Tepley, C. A., Janches, D., Friedman, J. S., Zhou, Q., & Mathews, J. D. (2004). Lidar observations of Ca and K metallic layers from Arecibo and comparison with micrometeor sporadic activity. *Journal of Atmospheric and Solar-Terrestrial Physics*, *66*(6–9), 595–606. https://doi.org/10.1016/j.jastp.2004.01.030

Roddy, P. A., Earle, G. D., Swenson, C. M., Carlson, C. G., & Bullett, T. W. (2004). Relative concentrations of molecular and metallic ions in midlatitude intermediate and sporadic-E layers. *Geophysical Research Letters*, *31*(19), L19807. https://doi.org/10.1029/2004GL020604

Smith, E. K. (1978). Temperate zone sporadic-E maps (f_oEs>7MHz). *Radio Science*, *13*(3), 571–575. https://doi.org/10.1029/RS013i003p00571

Tsuda, T. T., Chu, X., Nakamura, T., Ejiri, M. K., Kawahara, T. D., Yukimatu, A. S., & Hosokawa, K. (2015). A thermospheric Na layer event observed up to 140 km over Syowa Station (69.0°S, 39.6°E) in Antarctica. *Geophysical Research Letters*, *42*(10), 3647–3653. https://doi.org/10.1002/2015GL064101

Wang, J., Yang, Y., Cheng, X., Yang, G., Song, S., & Gong, S. (2012). Double sodium layers observation over Beijing, China. *Geophysical Research Letters*, *39*(15), L15801. https://doi.org/10.1029/2012GL052134

Wu, F., Chu, X., Du, L., Jiao, J., Zheng, H., Xun, Y., et al. (2022). First simultaneous lidar observations of thermosphere-ionosphere sporadic Ni and Na (TISNi and TISNa) layers (~105–120 km) over Beijing (40.42°N, 116.02°E) (Version 2) [Dataset]. Mendeley Data. https://doi.org/10.17632/scnxzsyj92.2

Wu, F., Zheng, H., Yang, Y., Cheng, X., Li, F., Du, L., et al. (2021). Lidar observations of the upper atmospheric nickel layer at Beijing (40°N, 116°E). *Journal of Quantitative Spectroscopy & Radiative Transfer*, *260*, 10748. https://doi.org/10.1016/j.jqsrt.2020.107468

Xue, X. H., Dou, X. K., Lei, J., Chen, J. S., Ding, Z. H., Li, T., et al. (2013). Lower thermospheric enhanced sodium layers observed at low latitude and possible formation: Case studies. *Journal of Geophysical Research: Space Physics*, *118*(5), 2409–2418. https://doi.org/10.1002/jgra.50200

Xun, Y., Yang, G., She, C. Y., Wang, J., Du, L., Yan, Z., et al. (2019). The first concurrent observations of thermospheric Na layers from two nearby central midlatitude lidar stations. *Geophysical Research Letters*, *46*(4), 1892–1899. https://doi.org/10.1029/2018GL081645

Yuan, T., Wang, J., Cai, X., Sojka, J., Rice, D., Oberheide, J., & Criddle, N. (2014). Investigation of the seasonal and local time variations of the high-altitude sporadic Na layer (Nas) formation and the associated midlatitude descending E layer (Es) in lower E region. *Journal of Geophysical Research: Space Physics*, *119*(7), 5985–5999. https://doi.org/10.1002/2014JA019942